ARTICLE

Effect of Gamma Irradiation on the Physical Properties of MoS₂ Monolayer

Received 00th January 20xx, Accepted 00th January 20xx

DOI: 10.1039/x0xx00000x

Chintan P Chavda^a, Ashok Srivastava^{a,e}, Erin Vaughan^b, Jianwei Wang^f, Manas Ranjan Gartia ^{c,*}, and Georgios Veronis ^{a,d,*}

Two-dimensional transition metal dichalcogenides (2D-TMDs) have been proposed as novel optoelectronic materials for space applications due to their relatively light weight. MoS₂ has been shown to have excellent semiconducting and photonic properties. Although the strong interaction of ionizing gamma radiation with bulk materials has been demonstrated, understanding its effect on atomically thin materials has scarcely been investigated. Here, we report the effect of gamma irradiation on the structural and optical properties of a monolayer of MoS₂. We perform Raman spectroscopy and X-ray photoelectron spectroscopy (XPS) studies of MoS₂, before and after gamma ray irradiation with varying doses and density functional theory (DFT) calculations. The Raman spectra and XPS results demonstrate that point defects dominate after the gamma irradiation of MoS₂. DFT calculations elucidate the electronic properties of MoS₂ before and after irradiation. Our work makes several contributions to the field of 2D materials research. First, our study of the phonon density of states and the electronic properties of a MoS₂ monolayer irradiated by gamma rays sheds light on the properties of a MoS₂ monolayer under gamma irradiation. Second, our study confirms that point defects are formed as a result of gamma irradiation. And third, our DFT calculations qualitatively suggest that the conductivity of the MoS₂ monolayer may increase after gamma irradiation due to the creation of additional defect states.

Introduction

Because of aggressive technology scaling, the channel length of silicon transistors is currently smaller than 8nm¹. High leakage current in silicon transistors ²⁻⁴ at smaller technologies leads to subthreshold swing of up to 60mV/decade⁵. Two-dimensional (2D) transition metal dichalcogenides (TMDs) have demonstrated their promising semiconducting and optical properties^{6, 7}. 2D TMD materials have good potential to lead to transistors with ultra-small channel length because of their promising applications in atomic layer devices ⁷⁻¹⁴. MoS₂ is one of the most promising TMD materials ^{6, 15-17}. Graphene is one of the most widely studied 2D materials but is challenging to be used as a channel material for switching devices

since it has no bandgap and a semimetal behaviour $^{18-21}$. In contrast, TMD materials, such as MoS_2 , $MoSe_2$, WS_2 , and WSe_2 , have bandgaps and show outstanding potential for future semiconductor-based devices because of their semiconducting properties $^{22-27}$. TMD materials have also been proposed for space applications and for biomedical devices 28 , 29 . In the space environment, there are many particles such as α and β particles, gamma rays, electrons, protons, and heavy ions. These energetic particles are expected to have strong interactions with materials $^{30-32}$. Radiation-induced defects in MoS_2 , such as vacancies, interstitials, and adatoms, affect its electrical, optical, and magnetic properties $^{33-37}$. It is therefore essential to analyse and understand the formation of these defects in MoS_2 and the relation to their semiconducting and optical properties.

Some studies have been done on irradiation effects on $MoS_2^{31, 36, 38-42}$. Ozden *et al.* investigated gamma irradiation effects on bulk MoS_2^{38} . He *et al.* investigated heavy ion (500 keV Au⁺ ion) radiation effects on a monolayer of MoS_2^{39} . Ghorbani-Asl *et al.* performed computational studies using molecular dynamics and DFT to investigate the effect of ion (He, Ne, Ar, Kr, Xe) radiation on a monolayer of MoS_2^{40} . Cheng *et al.* investigated the properties of the natural MoS_2 single crystal irradiated by medium- (1 MeV) and high-(357 MeV) energy Ni ions⁴¹. Wu *et al.* investigated electron irradiation effects on a monolayer of MoS_2 , using electron beam in a Raith eLINE lithography system⁴². Parkin *et al.* studied the Raman

Division of Electrical and Computer Engineering, Louisiana State University, Baton Rouge, LA, USA. E-mail: cchavd2@lsu.edu

b. United States Airforce Research Laboratory, Albuquerque, NM, USA. E-mail: erin.vaughan.1@us.af.mil

Department of Mechanical and Industrial Engineering, Louisiana State University, Baton Rouge, LA, USA. E-mail: mgartia@lsu.edu

d. Center for Computation and Technology, Louisiana State University, Baton Rouge, LA, USA. E-mail: gveronis@lsu.edu

e. Deceased.

Department of Geology and Geophysics, Louisiana State University, Baton Rouge, LA, USA. E-mail: jianwei@lsu.edu

[†] Electronic Supplementary Information (ESI) available: [details of any supplementary information available should be included here]. See DOI: 10.1039/x0xx00000x

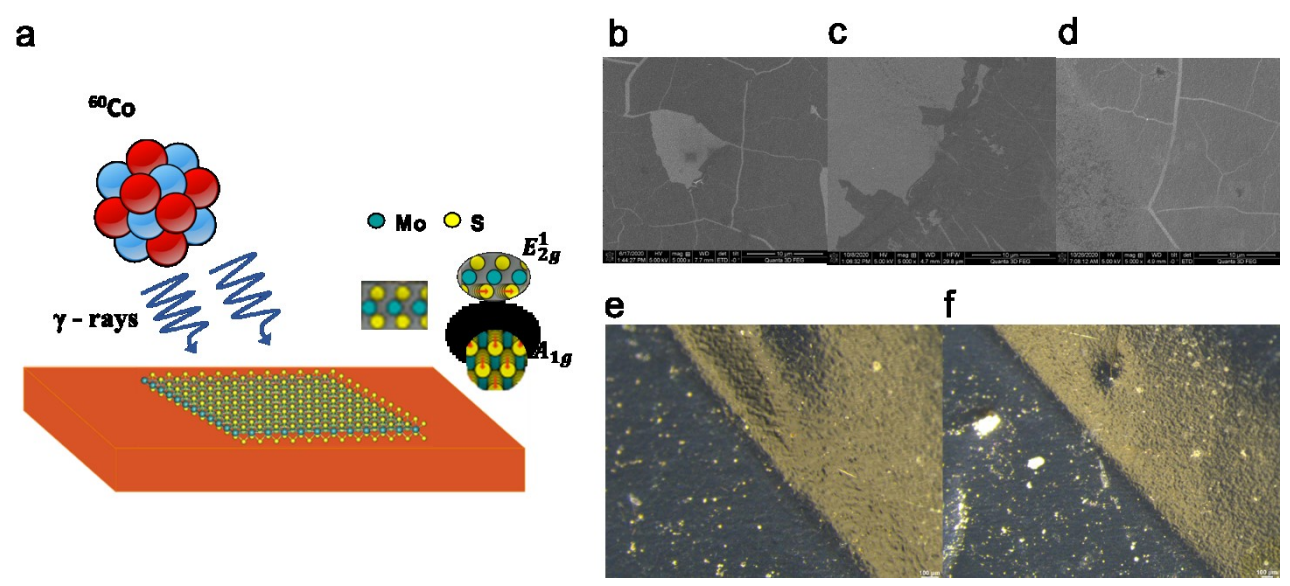


Figure 1. (a) Gamma irradiation on monolayer MoS_2 over copper substrate. (b) SEM image of pristine MoS_2 .[make scale bars visible] (c) SEM image of irradiated MoS_2 with 1.92 kGy. (d) SEM image of irradiated MoS_2 with cumulative dose of 5.30 kGy. (e) Optical image of pristine MoS_2 . (f) Optical image of irradiated MoS_2 with cumulative dose of 6.0 kGy.

spectra changes of electron irradiated MoS_2 using TEM with 200 kV⁴³. Tang *et al.* investigated fast neutron (1.2 MeV) irradiation effects on a monolayer of MoS_2^{44} . However, none of these studies were about gamma irradiation effects on a monolayer of MoS_2 .

In this work, we study gamma irradiation effects on a monolayer of MoS_2 . We investigate the electronic properties of irradiated MoS_2 by Raman spectroscopy and X-ray photoelectron spectroscopy (XPS). In our studies, we use a ^{60}Co source for irradiation purposes, which has a nominal irradiation dose of 1.91 Gy/min ($\pm 5\%$). Our experimental design includes samples of single and multiple (cumulative) irradiation doses. Further, we perform density functional theory (DFT) studies to theoretically investigate the electronic properties of defective monolayers of MoS_2 .

Materials and Methods

Monolayers of MoS_2 grown with chemical vapor deposition (CVD) over nickel-coated copper substrates were purchased from a 2D materials shop (6Carbon Technology). The 60 Co source at the Louisiana State University Nuclear Science building was used to irradiate the materials. The source has a nominal radiation dose rate of 1.91 Gy/min ($\pm 5\%$). 4 samples were used and assigned a number # 1, 2, 3 and 4. The gamma irradiation dose was 1.92 kGy, 1.92 kGy, 2.65 kGy, and 3.0 kGy for samples # 1, 2, 3, and 4, respectively. After two weeks, samples # 1, 2, 3, and 4 were subjected to an additional dose of 1.0 kGy, 1.75 kGy, 2.65 kGy, and 3.0 kGy, respectively. After these irradiation doses, we performed Raman spectroscopy, XPS, and scanning electron microscopy (SEM) studies.

Gamma Irradiation Setup

Supporting Figure S1 shows the schematic of the gamma irradiation experimental setup. We use a dry irradiator with a 60 Co source to

irradiate the samples. Decay-corrected dose rates were calculated to determine the required irradiation time for the different samples. All samples were placed at the same position in the irradiator chamber to ensure geometrical uniformity. The samples were placed five inches from the source, based on the manufacturer's recommendations for the irradiator. The dose rate was measured to be 191.72 rad/min. The dose rate remained the same after two weeks when we performed the cumulative irradiation dose experiments.

Raman Spectroscopy

We used a Renishaw inVia Reflex Raman spectroscope for the Raman experiments. We used a laser excitation wavelength of 532 nm in all experiments. The objective lens used was 50x, and the acquisition time was 10 seconds. We used the extended mode. The spectra were analysed using WiRE 5.3. We analysed its peaks using the OriginPro software suite.

X-ray Photoelectron Spectroscopy

We used a Scienta Omicron ESCA 2SR X-ray Photoelectron spectroscope for our XPS observations. It is equipped with a Mg/Al monochromatic source. The CASA XPS software package was used for the analysis of the XPS data.

DFT Calculations

DFT computational studies were performed using the Quantum Espresso Suite^{45, 46}. We perform DFT studies to investigate the electronic properties of pristine and irradiated monolayers of MoS₂.

substrate. Figures 2(a) and 2(b) show the Raman spectra after the first and second cumulative irradiation doses, respectively. At the

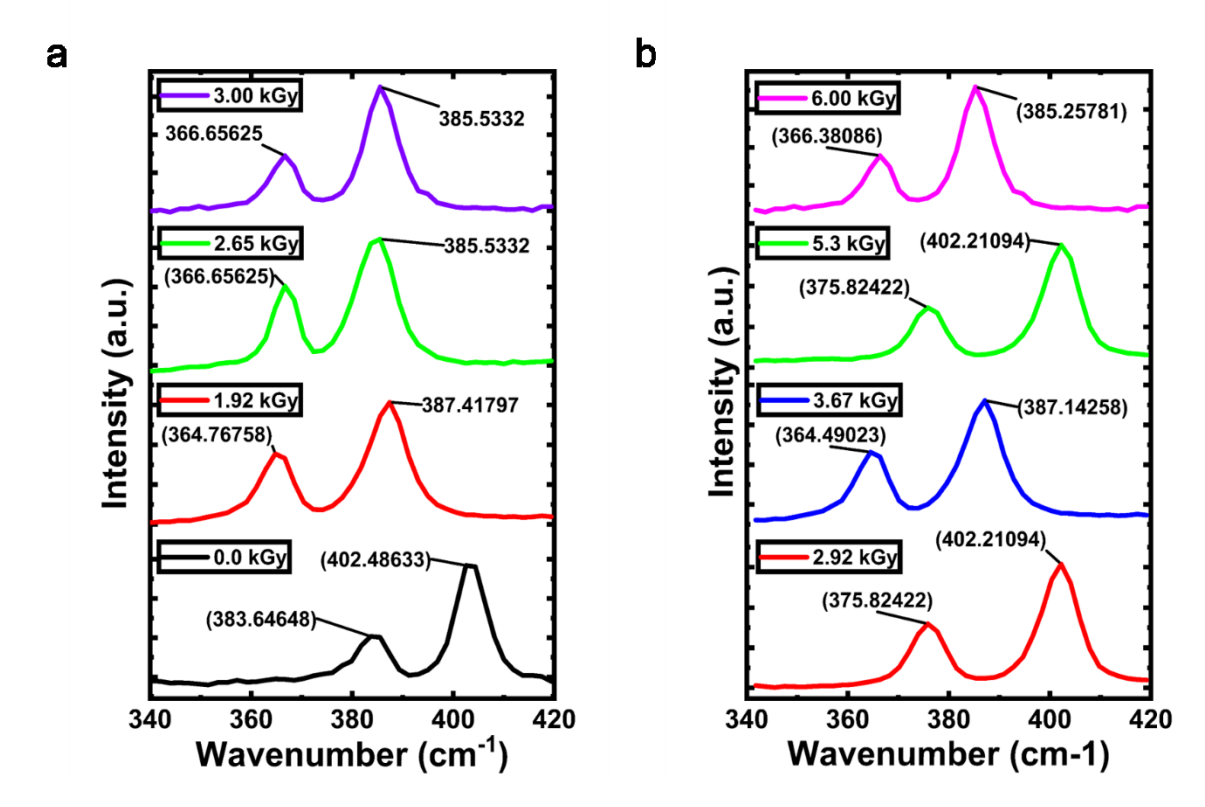


Figure 2.(a) Raman spectra of monolayer MoS_2 after the first set of irradiation doses. (b) Raman spectra results of monolayer MoS_2 after the second set of irradiation doses (cumulative doses).

Results and Discussion

Figure 1(a) schematically shows the interactions of gamma rays with MoS₂. Gamma ray irradiation plays an important role and contributes to pair production, Compton scattering, point defects of atoms (vacancies), and fast electrons⁴⁷. All of these may lead to changes in the structural and electronic properties of monolayer MoS₂. Common peaks in the Raman spectra of a monolayer of MoS₂ are E¹_{2g} (384.7 cm $^{\text{-}1}$), and A $_{\text{1g}}$ (403.6 cm $^{\text{-}1}$) at the Γ point in the Brillouin zone of a hexagon of monolayer MoS₂, according to group theory⁴⁸ (the schematic of the vibrations is shown in the inset of Fig. 1(a)). The E¹_{2g} mode is the result of the vibrations of two sulphur atoms with respect to the molybdenum atom, while the A_{1g} mode corresponds to the out-of-plane vibration of sulphur atoms in the opposite direction⁴⁸. The SEM images of the MoS₂ sample before (Fig. 1(b)) and after (Figs. 1(c) and 1(d)) gamma-ray irradiation did not show appreciable changes. The corresponding optical images are shown in Figs. 1(e) (before irradiation) and 1(f) (after irradiation).

Raman spectroscopy of irradiated MoS₂ monolayer

To describe the structural changes, we studied the Raman spectra of irradiated MoS_2 . The Raman spectra quantitatively describe the changes in the structural properties of monolayer MoS_2 . As mentioned in the Materials and Methods section, we use four samples of monolayer MoS_2 grown over a nickel-coated copper

excitation resonance condition of $\lambda=532$ nm, we observed two prominent peaks at 384.7 cm⁻¹ and 403.6 cm⁻¹ (Fig. 2(a)) corresponding to the E¹2g and A_{1g} vibrational modes, respectively⁴⁸. The Raman spectra corresponding to different irradiation doses are stacked vertically for clarity.

The change of Raman spectra as a function of irradiation is complicated. The E¹_{2g} peak Raman shift as a function of irradiation dose is plotted in Fig. 3(c). After an irradiation dose of 1.92 kGy, both the E¹_{2g} and A_{1g} peaks are red-shifted to a lower Raman frequency (Fig. 3(a) for E_{2g}). For single doses of 2.65 kGy and 3.0 kGy of irradiation, a minor blue shift of the Raman frequency occurs compared to the Raman frequency at 1.92 kGy, although these Raman frequencies are still red-shifted compared to the pristine MoS₂ sample (Fig. 3(c)). Fig. 3(c) shows the effect of cumulative doses on the Raman spectra. The cumulative doses show a zig-zag pattern with Raman frequencies jumping from a red shift to a blue shift repetition pattern with increased doses. After 3.67 kGy of gammaray irradiation, a redshift appears on the E¹2g and A_{1g} intensity peaks compared to 2.92 kGy. With further irradiations, blueshift and redshift appear after 5.30 kGy and 6.00 kGy, respectively (Fig. 2(b)). Previous DFT calculations showed that S vacancy defects lead to redshift in the E¹2g and A_{1g} peaks. In contrast, Mo vacancy defects lead to blueshift in the E12g and A1g peaks of the Raman spectra for

both monolayer and bulk MoS₂⁴⁹. As such, the irradiation can cause both red and blue shifts of the Raman peaks.

In previous studies, experimental observation suggested that removing the S atom (i.e., an S vacant) leads to weaker vibrations of the Mo-S restoring force⁵⁰. As a result, the E^1_{2g} band shifts to a lower phonon frequency (red shift). In other words, the red shift in the E^1_{2g}

was observed that the position of the A_{1g} mode is sensitive to doping (ion implantation/radiation)⁵². These point to the possible formation of S and Mo point defects in the monolayer of MoS₂.

The proposed scheme can also explain the peak intensity, peak intensity ratio, and peak width of the Raman spectra. Figure 3(a) shows the E^1_{2g} peak intensity as a function of irradiation dose. The black curve is for single-dose experiments, and the red curve is for

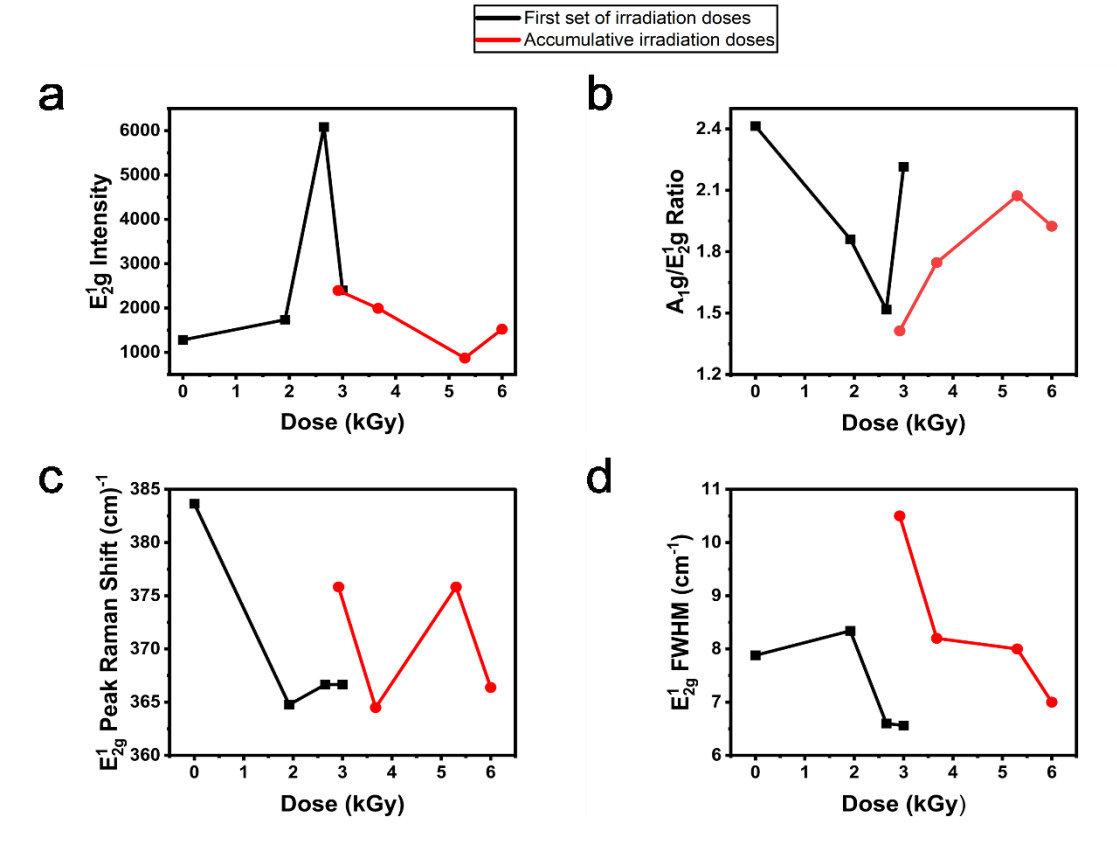


Figure 3. (a) E^{1}_{2g} peak intensity as a function of irradiation dose. (b) A_{1g}/E^{1}_{2g} peak intensity ratio as a function of irradiation dose. (c) E^{1}_{2g} peak Raman shift as a function of irradiation dose. (d) E^{1}_{2g} peak full width half maximum (FWHM) as a function of irradiation dose.

mode is caused by the dominance of S vacant defects in the monolayer of MoS₂. The red-shift of the E^1_{2g} peak could also be due to the effect of tensile strain in a few layers of atomically thin MoS₂ due to irradiation-induced defects⁵⁰. Thus, the red-shift observed in our spectra could be attributed to the effects discussed by Castellanos-Gomez *et al.* ⁵⁰. In our study, we also observe a red-shift of the A_{1g} peak. This could be due to a wrinkled MoS₂ layer⁵⁰, which is again caused by strain.

Based on our results, we propose that after the first irradiation dose, S defects dominate in both cases (first set of irradiation dose of 1.92 kGy and initial cumulative irradiation dose of 2.92 kGy). This is reasonable because the S atom is lighter than the Mo atom, so that it will be evicted first⁴³. As we increase the irradiation doses, we observe both kinds of shift (red shift and blue shift) in cumulative irradiation doses (Figs. 2(a) and 2(b)). This proposed scheme is also consistent with a previous study regarding radiation-induced defects in 2D materials. These defects are usually associated with doping and stress-strain⁵¹, and the radiation affects the vibrational A_{1g} mode⁵². It

cumulative-dose experiments. The E^1_{2g} peak intensity increases for doses up to 2.65 kGy, then decreases when the single dose increases from 2.65 to 3.0 kGy. Doses higher than 2.65 kGy of gamma irradiation decrease the E^1_{2g} peak intensity (for single dose and accumulative dose), which could be due to the formation of more defects leading to extra strain in the atomic structure of the monolayer of MoS₂. Literature data show that the extra strain is generally responsible for the degradation of the E^1_{2g} peak^{53,54} due to phonon softening in the monolayer of MoS₂ by point defects. It has been reported for graphene that moiré patterns can induce the vibrational properties revealed by the Raman spectra⁵⁵. The degradation of the E^1_{2g} mode is likely the result of a complex interplay of moiré-induced local strain and out-of-plane interaction with the substrate (Cu)⁵⁴.

In Fig. 3(b), we show the intensity ratio of the A_{1g} and E^{1}_{2g} peaks as a function of irradiation dose. Initially, with 1.92 kGy of irradiation dose, A_{1g}/E^{1}_{2g} decreases. This is the result of missing S atoms⁵⁶. Missing S atoms result in the relative decrease of the A_{1g} mode^{49,50,56,57}. Degradation in A_{1g}/E^{1}_{2g} is due to the competition between the effects of crystallinity and charge density^{52,58}. The introduction of

defects in the MoS₂ lattice by gamma irradiation leads to a decrease in the crystallinity, affecting the A_{1g} mode intensity. The defects also lead to changes in the charge density, which can affect both the A_{1g} and E_{2g} modes^{43, 50-55}. As we increase the irradiation dose, after 3.0 kGy of irradiation dose, the $A_{1g}/\ E^{1}_{2g}$ intensity increases, which may be due to the appearance of Mo vacancies for gamma irradiation doses higher than 2.65 kGy⁵⁹. The A_{1g}/E_{2g}^1 intensity ratio feature in the Raman spectra of irradiated MoS_2 samples shows that at low irradiation doses (1.92 kGy, 2.65 kGy) the S defects dominate⁴³. Figure 3(c) shows the E¹₂g Raman shift as a function of irradiation dose. Shift to lower frequencies (red shift) in Raman peaks, and especially in the E12g peak, indicates large cluster removal, such as MoS_4 or MoS_6^{53} . The intensity ratio $A_{1g}/$ E^1_{2g} and the E^1_{2g} Raman shift (Figs. 3(b) and 3(c)) suggest the formation of point defects by the gamma radiation⁶⁰. Unlike the results previously shown in the literature^{49, 53}, we did not find defect-induced Raman peaks at the lower frequency side of the E¹_{2g} peak.

In Fig. 3(d) we show the full width at half maximum (FWHM) of the E^1_{2g} peak as a function of irradiation dose. We observe that the FWHM of the E^1_{2g} peak decreases with the increase of radiation doses. The mechanical stress and strain in the structure are responsible for the degradation in the FWHM of the E^1_{2g} peak^{53, 57}. Literature data^{53, 57, 60} also suggest that the linewidth of the E^1_{2g} peak decreases with the increment of point defects by ion radiation and mechanical strain. Degradation of the E^1_{2g} mode occurred by creating S-vacancies through breaking the S-Mo-S bonds of MoS₂ by gamma irradiation, which facilitates the chemisorption of foreign molecules, in our case atmospheric oxygen⁵⁹.

XPS of irradiated MoS₂ monolayer

The XPS spectra are plotted for the gamma irradiated monolayer of MoS₂ (Fig. 4). In the spectra of pristine MoS₂ XPS study, we found peaks for nickel, oxygen, and carbon, which are either from impurity or slight contaminants in the instrument. Our samples are CVDgrown MoS₂ over nickel coated copper; hence Ni and Cu peaks appear in the survey spectra. The carbon peak is due to the presence of hydrocarbon in the XPS instrument itself and was utilized to calibrate the system. The peaks at 229.1 eV and 232.3 eV observed in the XPS spectra of pristine molybdenum are identified as Mo 3d_{5/2} and Mo 3d_{3/2}, respectively, and the small shoulder around 226 eV in Fig. 4(a) is the sulphur 2s peak. The locations of these peaks reflect the molybdenum atoms' chemical surroundings. The molybdenum atoms, in this instance, appear to be in the +4 oxidation state in accordance with the MoS_2 chemical formula. Mo $3d_{5/2}$ and Mo $3d_{3/2}$ are valence states of Mo, which is a characteristic of Mo species⁶¹. A small shoulder around 226 eV in the XPS spectra of pristine MoS₂ corresponds to the sulfur 2s peak. The presence of this peak further confirms the chemical identity of the monolayer MoS₂ and provides information on the sulfur atoms' chemical environment. In the pristine MoS_2 spectra of XPS, S consists of S $2p_{3/2}$ and S $2p_{1/2}$ peaks at 162 eV and 163.2 eV, respectively (Fig. 4(e))⁶². The locations of these peaks reflect the sulfur atoms' chemical environment in the MoS₂. The peak positions show that the sulfur atoms are in the -2 oxidation state, which is consistent with the chemical composition of MoS₂⁶⁰.

The evolution of Mo and S peaks at different doses are shown in Figs. 4(b)-4(d), and Figs. 4(f)-4(h), respectively.

We show the integrated peak area of XPS spectra for different atoms as a function of irradiation dose in Fig. 5(a). We observe that with the gamma irradiation the XPS peak area for both atom types (Mo and S) is decreasing after an initial dose of 1.92 kGy irradiation, and remains almost constant with higher irradiation doses of 2.65 kGy. For cumulative doses, the area of both atom types decreases for irradiation doses from 2.92 kGy to 3.67 kGy. These results imply that gamma irradiation modifies the monolayer MoS₂ sample, resulting in modifications to the XPS peak regions for the Mo and S atoms. The initial drop in peak area could result from alterations to the MoS₂ chemistry, leading to non-stoichiometric material caused by vacant defects or new chemical species (e.g., reduction of Mo or S). For instance, an S vacant can induce two localized electrons, which can cause a reduction of the neighboring Mo or S atom. The decline in peak regions seen for cumulative double doses may indicate that gamma irradiation effects are cumulative, causing more alterations and damages in the sample's chemical environment with increasing exposure⁶³.

Figures 5(b) and 5(c) show the changes in Mo and S XPS peak positions as a function of irradiation dose. The Mo 3d peak positions do not show appreciable changes after irradiation doses (Fig. 5(b)). This shows that under gamma radiation, the Mo atoms in the MoS₂ sample are reasonably stable, which suggests that the Mo valance state is more or less intact and some of the S atoms may be reduced as a result of S vacancy. The S $2p_{3/2}$ peak shows blue shift to higher binding energy after 1.92 kGy of irradiation compared to the no radiation case; however, for the cumulative doses of gamma radiation samples, we observe red shift of the XPS peaks to lower binding energy on the S 2p_{3/2} peak for all samples (Fig. 5(c)). The S $2p_{1/2}$ peak shows a similar trend with the irradiation doses. This indicates that the chemical environment of the S atoms is changing as a result of gamma irradiation, with the appearance of S defects. These results suggest that as the irradiation dose increases, S defects occur first, and with increased irradiation, Mo defects occur later. This is consistent with previous studies of defects in MoS₂ samples introduced through ion or electron irradiation which result in changes in the S XPS peak positions and peak areas⁶⁴.

In Fig. 5(d), we show the FWHM for different peaks of the MoS $_2$ XPS spectra as a function of irradiation dose. By the first 1.92 kGy of irradiation, the FWHM of S $2p_{3/2}$ and Mo $3d_{3/2}$ increases. The FWHM trend of S $2p_{3/2}$ and Mo $3d_{3/2}$ suggests that the quality of MoS $_2$ is degraded because of gamma irradiation⁶⁵. In addition, the trend in the FWHM for these peaks indicates that the gamma irradiation is inducing defects in the MoS $_2$ sample, resulting in increased disorder and reduced crystallinity. This is consistent with a previous study of Raman spectra that showed that gamma irradiation could lead to defects in 2D materials, resulting in increased disorder and reduced crystallinity⁶³. Overall, the XPS results suggest that gamma irradiation can induce changes in the chemical and structural properties of MoS $_2$

monolayer, leading to the appearance of defects and reduced quality.

irradiation dose, Mo defects are also appearing. After even higher irradiation doses of 2.65 kGy and 5.3 kGy (cumulative), S defects are more in quantity. The same trends are observed in the cumulative dose studies (Fig. 5(b), red curve). S defects are more likely to be dominant because S atoms are lighter than Mo atoms 66 . From the areas of the Mo 3d_{3/2} and S 2p_{3/2} peaks, we calculate the Mo:S atomic ratio $R_{\text{Mo-S}}$ as

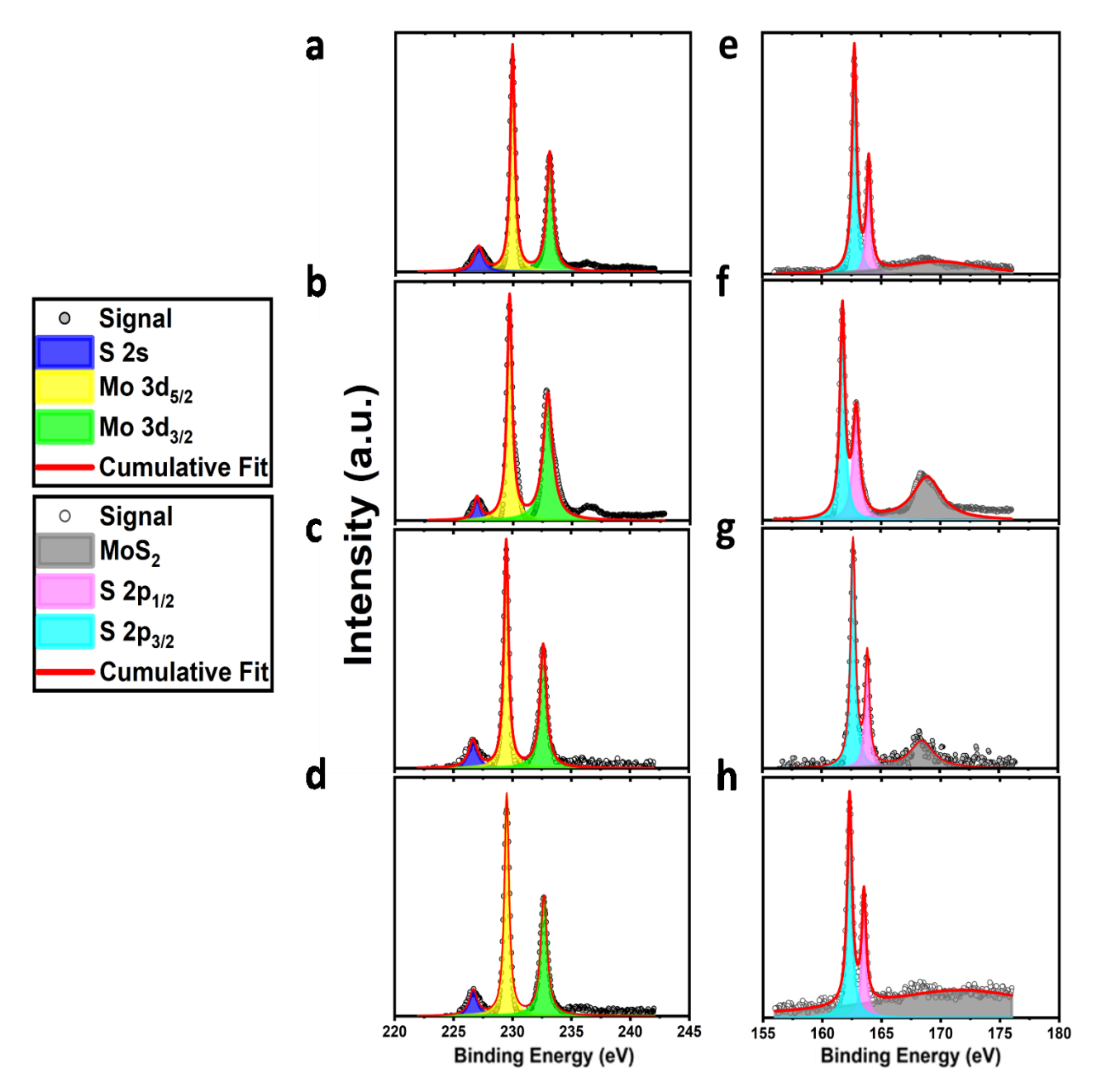


Figure 4. XPS spectra of MoS_2 . Mo d components with (a) 0 kGy; (b) 1.0 kGy; (c) 1.75 kGy; (d) 2.65 kGy of irradiation. S 2p components with (e) 0 kGy; (f) 1.00 kGy; (g) 1.75 kGy; (h) 2.65 kGy of irradiation.

Further, we show the area ratio of Mo to S peak as a function of irradiation dose in Fig. 5(e). For the first set of irradiations, the molar area ratio of Mo/S decreases and after irradiation doses higher than 2.65 kGy, it increases. This trend suggests that initially S defects are formed by a small amount of irradiation, and, after increasing the

$$R_{Mo/S} = (A_{Mo}/F_{Mo})/(A_s/F_s),$$
 ...(1)

where A_{Mo} and A_S are the peak areas of the Mo $3d_{3/2}$ and S $2p_{3/2}$ peaks, respectively; F_{Mo} and F_S are relative sensitivity factors (RSFs) of the Mo $3d_{3/2}$ and S $2p_{3/2}$ peaks, respectively. RSFs are calculated

by the CasaXPS software. After the highest amount of irradiation in both cases (single dose of 3.0 kGy and cumulative dose of 6.0 kGy), we believe that MoS_2 becomes amorphous⁶⁵. We observe that, as the irradiation dose increases, the Mo $3d_{5/2}$, S $2p_{1/2}$, and S $2p_{3/2}$ peaks are moving towards higher binding energies on the XPS spectra. The S 2p peaks increase by 6% in intensity compared to the ones in the pristine sample (Fig. 5(a)). Our XPS study suggests that sulphur defects appear first in the MoS_2 structure at lower irradiation dose level, followed by Mo defects at higher irradiation.

with the Perdew–Burke-Ernzerhof functional in the Generalized Gradient Approximation (GGA)^{67, 68}. The GGA method is the preferred option for many materials science and chemical simulations because it strikes a fair balance between accuracy and computing effectiveness. The GGA is essential because it incorporates information on the electron density gradient to account for non-uniform electron distributions, which is crucial for bonding patterns. The kinetic energy for the plane-wave basis was cut off at 100 Ry. For S, a 0.0 magnetic state was initiated, while for Mo, a 0.2

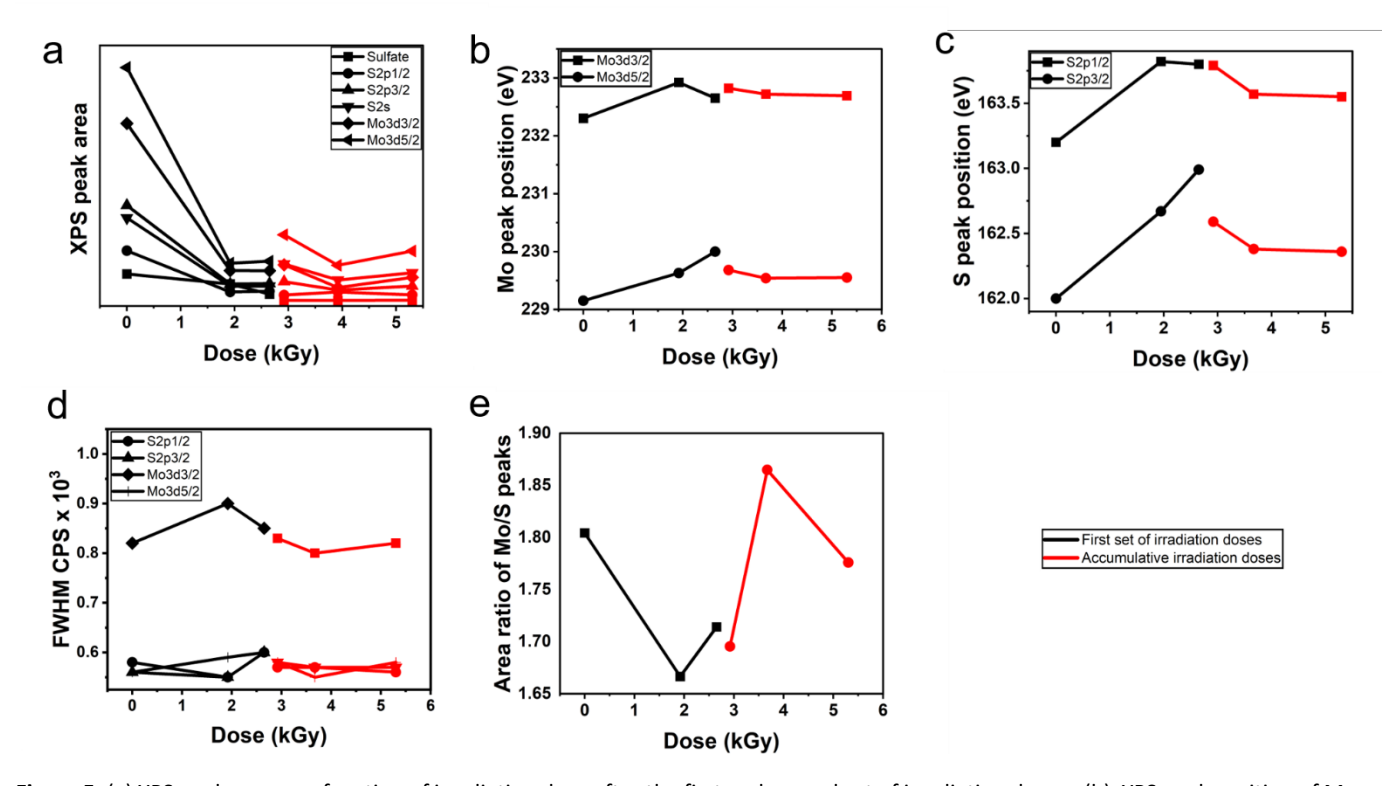


Figure 5. (a) XPS peak area as a function of irradiation dose after the first and second set of irradiation dose. (b) XPS peak position of Mo as a function of irradiation dose. (c) XPS peak position of S as a function of irradiation dose. (d) Full width at half maximum (FWHM) of XPS peaks as a function of irradiation dose. (e) Area ratio of Mo and S peaks as a function of irradiation dose.

Electronic Property Study

Our Raman spectra and XPS studies, as well as literature data ^{43, 49, 57}, suggest that point defects are the main defects in the MoS₂ structure after receiving irradiation doses. We examine the electronic properties of MoS₂ using DFT. More specifically, we perform DFT studies using the Quantum Espresso suite to obtain the electronic band structures of pristine and defective monolayer MoS₂. We perform our studies on a 5x5 supercell of monolayer MoS₂. The Quantum Espresso suite solves the Kohn-Sham equation to obtain the electronic properties of a system. The solution of the Kohn-Sham equation allows the Quantum Espresso suite to determine the band structure, density of states, and the charge density.

We used Density Functional Theory with plane wave basis sets as implemented in Quantum Espresso. We used exchange-correlation

magnetic state was initiated.

We performed a Quantum Espresso calculation on a pristine monolayer of MoS_2 structure with 75 atoms, a 5x5 cell size, 650 electrons, and 400 Kohn-Sham states. K-points were 12 12 12 0 0 0, and the convergence threshold was set to 1.00000e-06. Note that the convergence threshold is the highest permitted change in the total energy between two successive iterations of the self-consistent field (SCF) cycle. The relax approach, which only permits the variation of atomic locations, was used to carry out the optimization. The Brillouin zone is sampled using the k-points, and integrals over the reciprocal lattice vectors are computed using these points. Based on our results, the system was stable, and the optimization converged inside the predetermined threshold.

We used USPP-type pseudopotentials (Ultra-Soft Pseudopotentials) from the PS Library of Quantum Espresso. USPP pseudopotentials offer a more flexible description of the valence electrons by modeling

the ionic core using a smooth, soft pseudopotential that rapidly decays away from the nucleus. This pseudopotential has a smooth transition between the core and valence electrons as compared to normal pseudopotentials, which have an abrupt cutoff. One of the benefits of USPP are larger plane-wave basis sets, which are more adaptable and offer more accurate representations of the electronic structure. This leads to estimations of the total energy and the charge density that are more precise, particularly in systems with intricate bonding or in which relativistic effects play a significant role.

In Fig. 6(a) we show the atomic structure of pristine MoS₂, its band structure, and density of states. We found that the pristine MoS₂ has a bandgap of ~1.83 eV, which agrees with the literature reported value ⁶⁹. With the formation of defects, the bandgap decreases (Table S1). Figure 6(a) (middle figure) shows the band structure diagram of monolayer MoS2 with high symmetric points in the first Brillouin zone shown in the x-axis and the corresponding energy values in the y-axis. Since our experimental results suggested that at lower radiation doses S and Mo defects appear, we performed DFT simulations on the vacancy point defect structures of MoS₂ by removing 1S, 2S, and 1 Mo & 2S atoms in the supercell (Figs. 6(b)-6(d)). The 1S (Fig. 6(b)), and 2S (Fig. 6(c)) defects open narrow bandgaps of 1.03 eV and 0.98 eV, respectively. The bandgap value decreases with increase of defect concentration. This may lead to better conductivity in 2S defected MoS₂ compared to MoS₂ with 1S defect. With the formation of defects, the bands split and cross the Fermi energy level, as shown in the band diagrams. The Fermi energy of the defective MoS_2 is different from the one of pristine MoS_2 (Table S1). This is due to the movement of charge carriers in the structures as a result of the formation of the defects. We also show the corresponding total density of states (DOS) for each system (Figs. 6(a)-6(d), right). The DOS at Fermi energy (E = 0) for the pristine MoS₂ is zero, while for the defected MoS₂ the DOS is found to be non-zero. The simulations improve our understanding of the changes in the electronic structure of MoS₂ due to the creation of S and Mo vacancies.

Point defects in a monolayer of MoS_2 affect the band structure and density of states. For instance, in-gap states caused by the defects are observed in Figs. 6(b)-6(d). Their wavefunctions include hybridization between the p-orbitals of the surrounding Mo atoms and those of S^{70} . The bandgap of the defected MoS_2 (0.8 eV) [Fig. 6(d)] is substantially smaller than that of pristine MoS_2 (1.83 eV)⁷⁰ [Fig. 6(a)]. These transitions demonstrate how defects can affect the electronic structure of a monolayer of MoS_2^{70} .

In our DFT study, we observe the creation of new bands within bandgaps due to the defects in the monolayer structure of MoS_2 . We also found that, for the mono-sulfur vacant defect, bands that are created within the bandgap are occupied [Fig. 6(b)]. We also obtained similar results for two S defects and one Mo defect [Fig. 6(d)]. These results suggest that there are electrons available for conduction in new bands. These results also confirm that the bandgap of the monolayer of MoS_2 is reduced by creating defects induced by gamma irradiation.

Trainer et al. studied the electronic properties of a monolayer of MoS₂ with Mo vacancies (VMo) using scanning tunneling microscopy and spectroscopy⁷⁰. Their findings indicate the presence of three ingap states, which computed real-space projections can accurately describe. Furthermore, they observed that these in-gap states related to VMo are shifted in energy, indicating that they exist in two distinct charged states. Although the electron acceptor vacancies they identified cannot fully account for the intrinsic n-type doping of the MoS₂ films, they alter the local electronic density of states of the monolayer of MoS₂ ⁷⁰. These experimental results corroborate our DFT computational results for MoS₂, demonstrating the occupancy of new in-gap states in the presence of S, 2S, Mo, and S₂ vacancies. The in-gap states associated with VMo alter the density of states of electrons in MoS₂, leading to changes in its electronic properties⁷⁰. The occupancy of new in-gap states in the presence of defects in our DFT computation also proves a change in electronic properties with the reduction of the bandgap with more available electron states. The bandgap that we calculated using DFT is in agreement with experimental results reported by Trainer et al. 70. This agreement reinforces the validity of our computational findings.

Conclusions

In conclusion, we investigated gamma irradiation effects on a monolayer of MoS_2 . We studied the changes in the physical properties of MoS_2 using Raman spectroscopy and XPS. The results showed that S defects dominate at lower irradiation doses (below 2.65 kGy), while more Mo defects appear at higher irradiation doses. The shifting of Mo 3d and S 2p peaks in the XPS spectra confirmed the presence of S and Mo point defects. DFT studies suggest that, as the gamma irradiation dose increases, the bandgap decreases. Our DFT calculations also qualitatively suggest that the conductivity of the MoS2 monolayer may increase after gamma irradiation due to the creation of additional defect states.

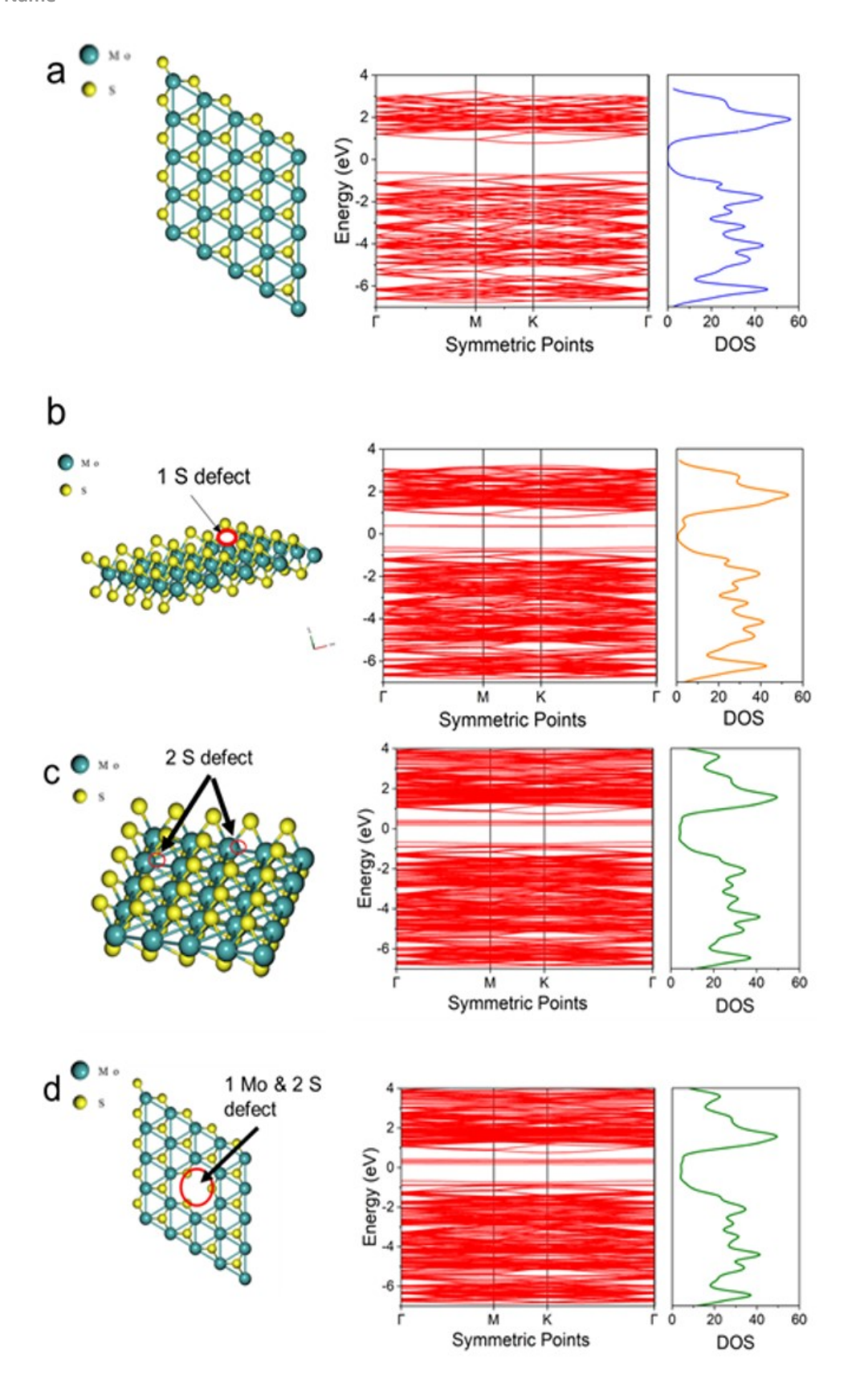


Figure 6. (a) Band structure and density of states of pristine MoS_2 . (b) Band structure and density of states of defected MoS_2 with two S defects. (c) Band structure and density of states of defected MoS_2 with one Mo and two S defects. (d) Band structure and density of states of defected MoS_2 with one Mo and two S defects.

Author Contributions

C.P.C, A.S., M.R.G., G.V., and E.V. conceived the project. C.P.C. performed all the experiments. C.P.C., M.R.G., J.W., and G.V. analysed the data and wrote the manuscript. M.R.G., J.W., G.V., and E.V. provided comments for the manuscript. G.V. and E.V. provided funding. A.S., M.R.G., G.V., and E.V. supervised the project.

Conflicts of interest

There are no conflicts to declare.

Acknowledgements

This work was partially supported by the United States Air Force Research Laboratory under agreement number FA9453-18-1-0103. M.R.G. is supported by the National Science Foundation (NSF CAREER award number: 2045640). The U.S. Government is authorized to reproduce and distribute reprints for Government purposes notwithstanding any copyright notation there on. The content in this publication has been approved for public release, PA Number AFRL20223302.

References

- N. Boukortt, S. Patanè and G. Crupi, Silicon, 2020, 12, 1585-1591.
- 2. K. F. Mak and J. Shan, *Nature Photonics*, 2016, **10**, 216-226.
- D. Lembke, S. Bertolazzi and A. Kis, Accounts of chemical research, 2015, 48, 100-110.
- 4. O. V. Yazyev and A. Kis, *Materials Today*, 2015, **18**, 20-30.
- 5. K. Babu and E. Goel, *Silicon*, 2022, 1-10.
- 6. M. Nayeri, M. Moradinasab and M. Fathipour, Semiconductor Science and Technology, 2018, **33**, 025002.
- 7. M. S. Ullah, A. H. B. Yousuf, A. D. Es-Sakhi and M. H. Chowdhury, Analysis of optical and electronic properties of MoS2 for optoelectronics and FET applications, 2018.
- 8. R. Walker, T. Shi, E. Silva, I. Jovanovic and J. Robinson, physica status solidi (a), 2016, 213, 3065-3077.
- 9. S. Dudarev, Annual Review of Materials Research, 2013, **43**, 35-61.
- J. Łażewski, P. Jochym, P. Piekarz, M. Sternik, K. Parlinski, J. Cholewiński, P. Dłużewski and S. Krukowski, *Journal of Materials Science*, 2019, 54, 10737-10745.
- 11. E. Engel and R. M. Dreizler, *Theoretical and mathematical physics*, 2011, 351-399.
- 12. J. F. Dobson, G. Vignale and M. P. Das, 2013.
- B. Doyle, R. Arghavani, D. Barlage, S. Datta, M. Doczy, J. Kavalieros, A. Murthy and R. Chau, *Intel Technology Journal*, 2002, 6.
- M. leong, B. Doris, J. Kedzierski, K. Rim and M. Yang, Science, 2004, 306, 2057-2060.
- 15. M. T. Bohr and I. A. Young, *IEEE Micro*, 2017, **37**, 20-29.
- 16. Y. Tan, L. Ma, Z. Gao, M. Chen and F. Chen, *Nano letters*, 2017, **17**, 2621-2626.
- Y. Yoon, K. Ganapathi and S. Salahuddin, *Nano letters*, 2011, 11, 3768-3773.

- A. C. Neto, F. Guinea, N. M. Peres, K. S. Novoselov and A. K. Geim, Reviews of modern physics, 2009, 81, 109.
- 19. K. Novoselov, S. Morozov, T. Mohinddin, L. Ponomarenko, D. Elias, R. Yang, I. Barbolina, P. Blake, T. Booth and D. Jiang, *physica status solidi (b)*, 2007, **244**, 4106-4111.
- 20. E. McCann and M. Koshino, *Reports on Progress in physics*, 2013, **76**, 056503.
- 21. F. Schwierz, *Nature nanotechnology*, 2010, **5**, 487-496.
- 22. H. Jiang, *The Journal of Physical Chemistry C*, 2012, **116**, 7664-7671
- D. Ovchinnikov, A. Allain, Y.-S. Huang, D. Dumcenco and A. Kis, ACS nano, 2014, 8, 8174-8181.
- A. L. Elías, N. Perea-López, A. Castro-Beltrán, A. Berkdemir,
 R. Lv, S. Feng, A. D. Long, T. Hayashi, Y. A. Kim and M. Endo,
 ACS nano, 2013, 7, 5235-5242.
- Y. Ma, Y. Dai, M. Guo, C. Niu, J. Lu and B. Huang, *Physical Chemistry Chemical Physics*, 2011, 13, 15546-15553.
- Y. Di Iorio, M. Berruet, D. Gau, E. Spera, C. Pereyra, R. Marotti and M. Vázquez, physica status solidi (a), 2017, 214, 1700191.
- R. Roldán, J. A. Silva-Guillén, M. P. López-Sancho, F. Guinea,
 E. Cappelluti and P. Ordejón, Annalen der Physik, 2014,
 526, 347-357.
- T. Vogl, K. Sripathy, A. Sharma, P. Reddy, J. Sullivan, J. R. Machacek, L. Zhang, F. Karouta, B. C. Buchler and M. W. Doherty, *Nature communications*, 2019, 10, 1-10.
- 29. A. J. Arnold, T. Shi, I. Jovanovic and S. Das, *ACS applied materials & interfaces*, 2019, **11**, 8391-8399.
- C. P. Chavda, A. Srivastava, S. K. Pradhan and M. Bahoura, Gamma irradiation effect studies on monolayer CVD grown graphene on metallic substrates, 2020.
- 31. C. P. Chavda, G. Veronis, A. Srivastava and E. Vaughan, Gamma irradiation effect studies on monolayer molybdenum disulfide on copper substrates, 2021.
- H. Li, C. Liu, Y. Zhang, C. Qi, Y. Wei, J. Zhou, T. Wang, G. Ma,
 H.-S. Tsai and S. Dong, *Nanotechnology*, 2019, 30, 485201.
- 33. B. Foran, C. Mann, M. Peterson, A. Bushmaker, B. Wang, J. Chen, S. Yang and S. B. Cronin, *IEEE Transactions on Nuclear Science*, 2018, **66**, 413-419.
- 34. B. Wang, S. Yang, J. Chen, C. Mann, A. Bushmaker and S. B. Cronin, *Applied Physics Letters*, 2017, **111**, 131101.
- 35. H. Yockell-Lelièvre, F. Lussier and J.-F. Masson, *The Journal of Physical Chemistry C*, 2015, **119**, 28577-28585.
- G.-Y. Zhao, H. Deng, N. Tyree, M. Guy, A. Lisfi, Q. Peng, J. A. Yan, C. Wang and Y. Lan, Applied Sciences, 2019, 9, 678.
- P. Kolhe, A. Thorat, A. Phatangare, P. Jadhav, S. Dalvi, S. Dhole and S. Dahiwale, *Journal of Alloys and Compounds*, 2022, 896, 162969.
- B. Ozden, M. P. Khanal, J. Park, S. Uprety, V. Mirkhani, K. Yapabandara, K. Kim, M. Kuroda, M. J. Bozack and W. Choi, Micro & Nano Letters, 2017, 12, 271-274.
- 39. Z. He, R. Zhao, X. Chen, H. Chen, Y. Zhu, H. Su, S. Huang, J. Xue, J. Dai and S. Cheng, ACS applied materials & interfaces, 2018, 10, 42524-42533.
- M. Ghorbani-Asl, S. Kretschmer, D. E. Spearot and A. V. Krasheninnikov, 2D Materials, 2017, 4, 025078.
- 41. L. Cheng, T. Liu, W.-J. Kong, Y. Liu, F.-R. Liu, Y.-F. Bao and P. Liu, *Results in Physics*, 2022, **34**, 105306.
- 42. X. Wu, Y. Gu, R. Ge, M. I. Serna, Y. Huang, J. C. Lee and D. Akinwande, npj 2D Materials and Applications, 2022, 6, 31.

68.

- W. M. Parkin, A. Balan, L. Liang, P. M. Das, M. Lamparski, C. H. Naylor, J. A. Rodríguez-Manzo, A. C. Johnson, V. Meunier and M. Drndic, ACS nano, 2016, 10, 4134-4142.
- G. Tang, M. E. Pam, H. Zhang, Z. Shu, P. Feng, B. Wei, L. Ang,
 H. Y. Yang and M. Li, Applied Physics Express, 2019, 12,
 056001.
- 45. K. F. Garrity, J. W. Bennett, K. M. Rabe and D. Vanderbilt, Computational Materials Science, 2014, 81, 446-452.
- P. Giannozzi, S. Baroni, N. Bonini, M. Calandra, R. Car, C. Cavazzoni, D. Ceresoli, G. L. Chiarotti, M. Cococcioni and I. Dabo, *Journal of physics: Condensed matter*, 2009, 21, 395502.
- 47. J. F. Felix, A. F. Da Silva, S. W. Da Silva, F. Qu, B. Qiu, J. Ren, W. M. De Azevedo, M. Henini and C.-C. Huang, *Nanoscale Horizons*, 2020, **5**, 259-267.
- 48. H. Li, Q. Zhang, C. C. R. Yap, B. K. Tay, T. H. T. Edwin, A. Olivier and D. Baillargeat, *Advanced Functional Materials*, 2012, **22**, 1385-1390.
- 49. S. Bae, N. Sugiyama, T. Matsuo, H. Raebiger, K.-i. Shudo and K. Ohno, *Physical Review Applied*, 2017, **7**, 024001.
- A. Castellanos-Gomez, R. Roldán, E. Cappelluti, M. Buscema, F. Guinea, H. S. van der Zant and G. A. Steele, Nano letters, 2013, 13, 5361-5366.
- 51. N. Blanc, F. Jean, A. V. Krasheninnikov, G. Renaud and J. Coraux, *Physical Review Letters*, 2013, **111**, 085501.
- B. Chakraborty, A. Bera, D. Muthu, S. Bhowmick, U. V. Waghmare and A. Sood, *Physical Review B*, 2012, 85, 161403.
- 53. H.-Q. Zhao, X. Mao, D. Zhou, S. Feng, X. Shi, Y. Ma, X. Wei and Y. Mao, *Nanoscale*, 2016, **8**, 18995-19003.
- 54. F. Tumino, C. S. Casari, M. Passoni, V. Russo and A. L. Bassi, *Nanoscale Advances*, 2019, **1**, 643-655.
- A. Eckmann, J. Park, H. Yang, D. Elias, A. S. Mayorov, G. Yu,
 R. Jalil, K. S. Novoselov, R. V. Gorbachev and M. Lazzeri,
 Nano letters, 2013, 13, 5242-5246.
- X. Luo, Y. Zhao, J. Zhang, Q. Xiong and S. Y. Quek, *Physical Review B*, 2013, 88, 075320.
- C. Rice, R. Young, R. Zan, U. Bangert, D. Wolverson, T. Georgiou, R. Jalil and K. Novoselov, *Physical Review B*, 2013, 87, 081307.
- S. Mignuzzi, A. J. Pollard, N. Bonini, B. Brennan, I. S. Gilmore, M. A. Pimenta, D. Richards and D. Roy, *Physical Review B*, 2015, 91, 195411.
- H. J. Kim, D. Kim, S. Jung, M. H. Bae, Y. J. Yun, S. N. Yi, J. S.
 Yu, J. H. Kim and D. H. Ha, *Journal of Raman Spectroscopy*, 2018, 49, 1938-1944.
- 60. D. Ganta, S. Sinha and R. T. Haasch, *Surface Science Spectra*, 2014, **21**, 19-27.
- 61. H. Wang, P. Skeldon and G. Thompson, *Surface and Coatings Technology*, 1997, **91**, 200-207.
- N. P. Kondekar, M. G. Boebinger, E. V. Woods and M. T. McDowell, ACS applied materials & interfaces, 2017, 9, 32394-32404.
- 63. R. Addou, L. Colombo and R. M. Wallace, *ACS applied materials & interfaces*, 2015, **7**, 11921-11929.
- 64. A. Pelella, O. Kharsah, A. Grillo, F. Urban, M. Passacantando, F. Giubileo, L. Iemmo, S. Sleziona, E. Pollmann and L. Madauß, *ACS Applied Materials & Interfaces*, 2020, **12**, 40532-40540.
- R. Zhang, L. Qiao, H. Zhang, X. Zhao, X. Gao and P. Wang, *Applied Surface Science*, 2022, 152497.

- H. Wang, L. Yu, Y.-H. Lee, Y. Shi, A. Hsu, M. L. Chin, L.-J. Li,
 M. Dubey, J. Kong and T. Palacios, *Nano letters*, 2012, 12,
 4674-4680.
- 67. P. E. Blöchl, *Physical review B*, 1994, **50**, 17953.
 - J. P. Perdew and Y. Wang, *Physical review B*, 1992, **45**, 13244.
- W. S. Yun, S. Han, S. C. Hong, I. G. Kim and J. Lee, *Physical Review B*, 2012, **85**, 033305.
- D. J. Trainer, J. Nieminen, F. Bobba, B. Wang, X. Xi, A. Bansil and M. Iavarone, npj 2D Materials and Applications, 2022, 6, 13.